Comparison of Dual-energy vs. Multi-energy Sinogram Decomposition Methods

Yaoshen Yuan, Brian Tracey, Eric Miller

Abstract

There is growing interest in developing X-ray computed tomography (CT) imaging systems with improved ability to discriminate material types, going beyond the attenuation imaging provided by most current systems. Dual-energy CT (DECT) systems can partially address this problem by estimating Compton and photoelectric (PE) coefficients of the materials being imaged, but DECT is greatly degraded by the presence of metal or other materials with high attenuation. Here we explore the advantages of multi-energy CT (MECT) systems based on photon-counting detectors. The utility of MECT has been demonstrated in medical applications where photon-counting detectors allow for the resolution of absorption K-edges. Our primary concern is aviation security applications where K-edges are rare. We simulate phantoms with differing amounts of metal (high, medium and low attenuation), both for switched-source DECT and for MECT systems, and include a realistic model of detector energy resolution. We extend the DECT sinogram decomposition method of Ying et al. to MECT, allowing estimation of separate Compton and photoelectric sinograms. We furthermore introduce a weighting based on a quadratic approximation to the Poisson likelihood function that deemphasizes energy bins with low signal. Simulation results show that the proposed approach succeeds in estimating material properties even in high-attenuation scenarios where the DECT method fails, improving the signal to noise ratio of reconstructions by over 20 dB for the high-attenuation phantom. Our work demonstrates the potential of using photon counting detectors for stably recovering material properties even when high attenuation is present, thus enabling the development of improved scanning systems.

1 Simulation Description

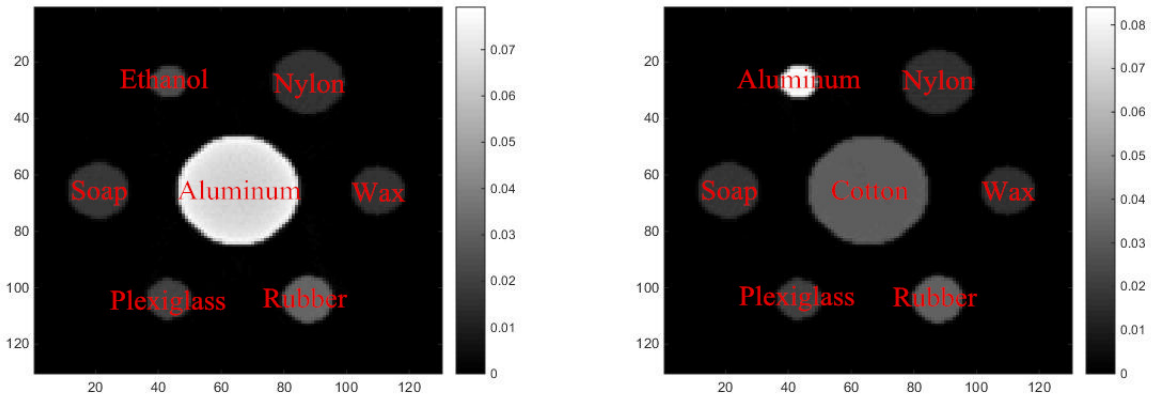

(a) High attenuation phantom

(b) Medium attenuation phantom

Figure 1: Phantom

Table 1: Both low and high energy source spectra are used for the realistic dual-energy simulation. Only a single high energy spectrum is used for other cases. Here we assume integrating detector is implemented for realistic dual-energy CT and photon counting detector with a varying number of energy bins is used for other simulations.

Case	Detector type	Spectra used	# of bins
Switched dual-energy (SwDE)	integrating	low and high energy spectra from Figure 3a	N/A
Ideal dual-energy (IdDE)	photon counting (no overlap)	high energy spectrum from Figure 3a	2
Ideal 7 bin	photon counting (no overlap)	high energy spectrum	7
Realistic 7 bin	photon counting (realistic overlap)	high energy spectrum	7

1.1 Phantoms

In this work, three different types of phantoms were used for simulation to explore how the amount of metal affects the accuracy of Compton and photoelectric (PE) reconstruction. First, we used a phantom (Figure 1a, called "high attenuation"), which includes aluminum, soap, ethanol, nylon, wax, rubber and plexiglass. This simulates the situation where a large amount of metal is in the phantom. The second phantom ("medium attenuation") has the same geometry but the middle circle is replaced by cotton and the small circle of ethanol is replaced by aluminum (Figure 1b), which represents the situation where a small amount of metal is present. In the third phantom ("low attenuation"), the aluminum circle in the first phantom is replaced by cotton to simulate the situation where there is no metal. The amount of metal actually does influence the accuracy of result as shown later.

1.2 Sources

To recover the Comptom and PE image, we used the spectra from the paper of Oguz Semerci and Eric L Miller [1]. The spectra consist of two individual spectra, a low-energy spectrum and a high-energy spectrum. The low-energy spectrum spans from 8 keV to 80 keV and the high-energy spectrum is from 14 keV to 139 keV (Figure 3a).

Often, dual energy CT (DE) is implemented using switched sources, where high-energy then low-energy source spectrum is switched electronically. The integrating detector will then measure the photons for each of the spectra. The left column of Table 1 explains the source spectra utilized in dual energy CT. In this paper, we call this approach 'Switched dual-energy', abbreviated 'SwDE'.

For other simulations, we will use only a single scan, which is identical to the high-energy scan from SwDE (the right column of Table 1). In these simulations, we assume the detector can discriminate photon energy. For multi-energy (ME) simulations, we may divide the spectrum into multiple evenly-spaced bins (7, 128, etc) to simulate photon-counting detectors. As a special case, we consider the case of 2 ideal bins, and call this 'ideal dual-energy', or 'IdDE'. The detailed description will be given in the next section.

Intuitively, it may be unclear how to compare SwDE and IdDE. However, the results show that IdDE performance is better than SwDE, even though IdDE only uses one scan while the SwDE is able to use a second scan, which provides more information about the phantom. This performance improvement shows the promise of photon-counting detectors.

1.3 Detectors

There are two different types of detectors used in the computed tomography (CT), namely integrating detectors and photon counting detectors. An integrating detector converts the electrical charge into the number of photons by amplification and digitalization. Integrating detectors do not give information on the energy of the detected photons. A photon counting detector transfers the photon into electrical pulse. The energy of the photon determines the amplitude of electrical pulse, by which the number of photons at specific energy bin can be determined [1].

For the ideal situation, because we assume that the detector can accurately classify the photon energy into its corresponding energy bin, the detector can perfectly divide the spectrum into several bins, meaning that there is no overlap between two consecutive bins. For instance, for the ideal 7 bins simulation, which was used in this paper, the spectrum will be evenly divided into 14 to 31 keV, 32 to 49 keV, ..., 127 to 139 keV(Figure 2b). No overlap exists between the bins.

However, superposition appears in realistic multi-energy detectors. For the realistic multi-bins, the model from E Roessl and C Herrmann [2] can nicely emulate the real situation using photon counting detector. A sensitivity function is added to the model to produce the overlapped spectrum (Figure 3b). In Figure 4, sensitivity function as well as Gaussian response function are shown given that Fano factor is 0.089 for sensor material CZT.

Different from the ideal model, this model takes a finite energy resolution into consideration. This can be described as follows:

$$\bar{\boldsymbol{Y}}_{\boldsymbol{l}} = \int_0^\infty S(E)\Omega_l(E)exp(-f_{KN}(E)\boldsymbol{A_c} - f_p(E)\boldsymbol{A_p})dE \tag{1}$$

where $\bar{\boldsymbol{Y}}_{\boldsymbol{l}}$ is the mean of Poisson random variable for the ith energy bin and $\Omega_i(E)$ is the sensitivity function for the ith energy bin. A photon with energy E can produce a signal with energy $E^{'}$. This can occur, for example, when two photons arrive nearly simultaneously, so the detector will detect the single photon with higher energy. In addition, the detector electronics are not perfectly able to measure photon energy. A Gaussian response function (Eq.2) is therefore introduced to obtain the sensitivity function. Namely, the detected energy of a photon is a Gaussian distribution whose mean is the true energy of the photon.

$$R(E, E^{'}) = \frac{1}{\sqrt{2\pi}\sigma_E} e^{-\frac{(E^{'}-E)^2}{2\sigma_E^2}} \tag{2}$$

where $\sigma_E = k\sqrt{E}$. Here $k = \sqrt{fano}$, where $fano$ is the Fano factor of the sensor material. Therefore, in order to simulate the spectrum for each energy bin, a Gaussian spectral response $R(E, E^{'})$ corresponding to each energy E should be integrated within the range of the energy bin. This integration is the sensitivity function.

$$\Omega_l(E) = \int_{E_l}^{E_{l+1}} R(E, E^{'})dE^{'} \tag{3}$$

where $\Omega_l(E)$ is the sensitivity function for lth bin.By multiplying the sensitivity function with the source spectrum, the spectrum for each bin can be obtained. Eq.1 shows the modified model for the realistic spectrum divided into multiple bins.

1.4 Simulated noise

For different detectors, different noise types were added in the simulation. Because photon counting detector employs the channel, which contains a comparator circuit and a counter, each time the pulse voltage exceeds the threshold of comparator, the counter is increased by one. Finally the number of photons detected above the threshold can be acquired [3]. The readout noise can be eliminated because photon counting detector does not transfer the accumulated voltage into photon number but utilizes the direct

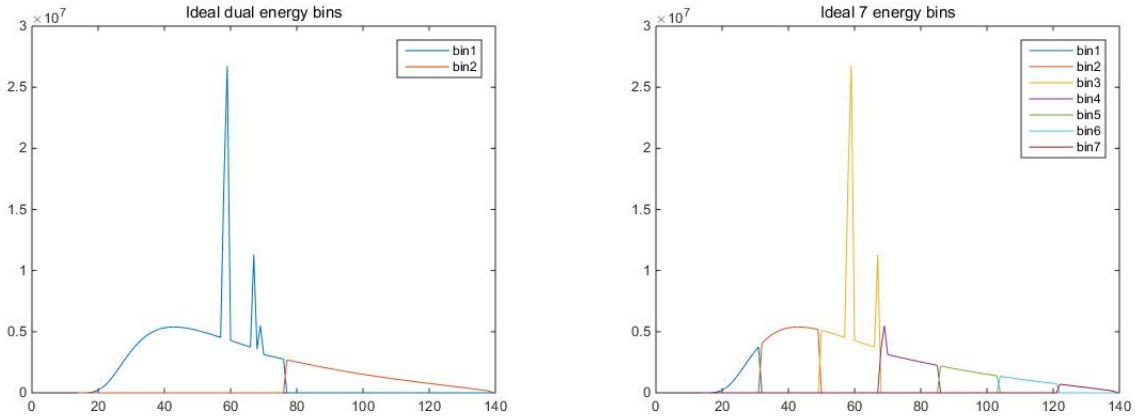

(a) Ideal spectrum for 2 bins (IdDE)

(b) Ideal spectrum for 7 bins

Figure 2: The figure shows the ideal case where the detected spectra can be ideally split into multiple bins for the ideal case. The left plot is the dual-energy spectrum and the right one is the multi-energy spectrum.

relation between photons and counter. Therefore, here we only used Poisson distribution for the multi-bins simulation [4].

In integrating detectors, the total energy accumulated by the incoming photons is integrated, thus random noise, such as thermal noise, will be produced by the electronic devices in the detector [5]. Gaussian noise is normally added to the photon detected, which can be described as follows [4]:

$$\boldsymbol{Y_L} = Poisson\{\bar{\boldsymbol{Y}}_{\boldsymbol{L}}\} + Normal(0, \sigma_{e,L}) \tag{4}$$

$$\boldsymbol{Y_H} = Poisson\{\bar{\boldsymbol{Y}}_{\boldsymbol{H}}\} + Normal(0, \sigma_{e,H}) \tag{5}$$

where σ_e is the variance of electronic noise, $\bar{\boldsymbol{Y}}_{\boldsymbol{L}}$ and $\bar{\boldsymbol{Y}}_{\boldsymbol{H}}$ are the means of Poisson random variable for low and high energy spectrum respectively, which are defined as:

$$\bar{\boldsymbol{Y}}_{\boldsymbol{L}} = \int S_L(E) exp(-f_{KN}(E)\boldsymbol{A_c} - f_p(E)\boldsymbol{A_p}) dE \tag{6}$$

$$\bar{\boldsymbol{Y}}_{\boldsymbol{H}} = \int S_H(E) exp(-f_{KN}(E)\boldsymbol{A_c} - f_p(E)\boldsymbol{A_p}) dE \tag{7}$$

where $\boldsymbol{A_c}$ and $\boldsymbol{A_p}$ are the Compton and photoelectric vectors composing the attenuation. $S_H(E)$ and $S_L(E)$ are the high and the low energy spectra.

For the case of dual-bins, an integrating detector was simulated so both Poisson and Gaussian noise (SNR=60 dB) were added to the number of photons detected. For the case of multi-bins, a photon counting detector was assumed to be used, so only Poisson noise was added in the simulation.

1.5 Processing

1.5.1 Sinogram decomposition

There are two factors that contribute to the X-ray attenuation in the energy range of interest. One is the Compton scattering, and another is the photoelectric effect [6]. The use of these two effects can help distinguish different materials because of their specific scattering and photoelectric properties. The attenuation coefficient $\mu(E)$ can then be represented by a linear combination of Compton a_c and photoelectric

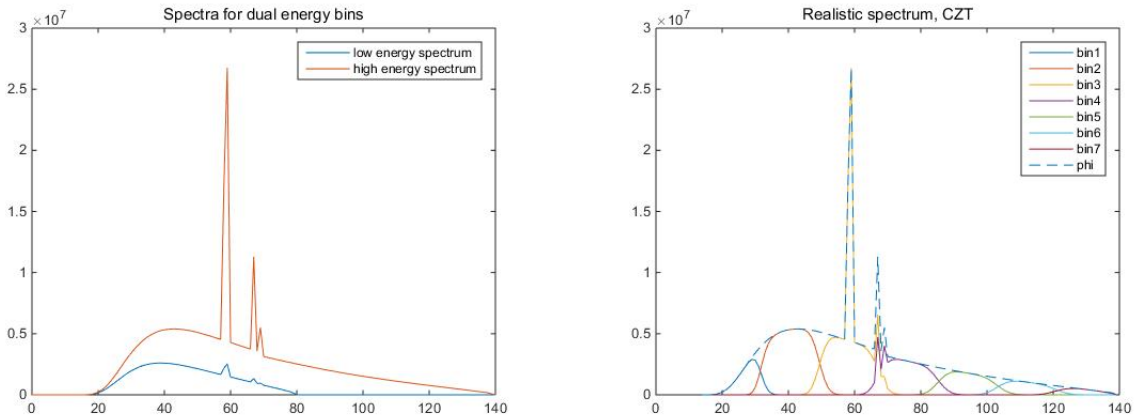

(a) Realistic spectrum for 2 bins (SwDE)

(b) Realistic spectrum for 7 bins

Figure 3: Realistic simulation cases. The left plot shows two independent source spectra for realistic dual-energy case (SwDE). The right plot shows a realistic photon counting detector splits the high energy spectrum (only high energy spectrum was used) into 7 bins imperfectly because of the finite energy resolution.

coefficient a_p. The relationship between attenuation and Compton as well as photoelectric coefficient can be defined as:

$$\mu(x, y; E) = a_c(x, y) f_{KN}(E) + a_p(x, y) f_p(E) \tag{8}$$

where (x,y) represents the coordinates and E stands for the incident energy. Function $f_p(E)$ and $f_{KN}(E)$ are called basis functions, which is related to the energy. $f_p(E)$ approximates the energy dependence of the photoelectric interaction, which is defined as:

$$f_p(E) = E^{-3} \tag{9}$$

$f_{KN}(E)$ is the Klein-Nishina function, meaning the energy dependence of total cross section for Compton scattering. It can be described as follows [6]:

$$f_{KN}(\alpha) = \frac{1+\alpha}{\alpha^2}\left[\frac{2(1+\alpha)}{1+2\alpha} - \frac{1}{\alpha} ln(1+2\alpha)\right] + \frac{1}{2\alpha} ln(1+2\alpha) - \frac{(1+3\alpha)}{(1+2\alpha)^2}. \tag{10}$$

Then we can convert a_c and a_p to the projection form A_c and A_p. A_c and A_p are the line integrals of a_c and a_p (Eq.11), so we can measure two independent projection values at each point. For the ith ray,

$$A_c^i = \int_{S_i} a_c(x, y) dl \qquad \text{and} \qquad A_p^i = \int_{S_i} a_p(x, y) dl \tag{11}$$

where S_i means the ith path. Therefore, the linear relationship between projection of attenuation and A_c and A_p is:

$$\int_{S_i} \mu(x, y) dl = A_c^i f_{KN}(E) + A_p^i f_p(E) \tag{12}$$

Because of the linear relation described above (Eq.12), we can recover A_c and A_p from the projection of attenuation. Here we used Ying's method [7] to decompose the dual energy as well as multiple energy projections into Compton and photoelectric projections. The reconstruction of A_c and A_p can be transferred to a constrained minimization problem, which finds the solution, A_c and A_p, to minimize the least square error between the measured projections and modeled projections. Here we define $\theta^i = \left[A_c^i, A_p^i\right]$. Thus for dual energy decomposition problem, the minimization of least square error can be described as:

$$\theta^i = \arg\min_{\theta^i} \underbrace{[K_L(\theta^i) - m_L^i]^2 + [K_H(\theta^i) - m_H^i]}_{Q_{\theta^i}} \tag{13}$$

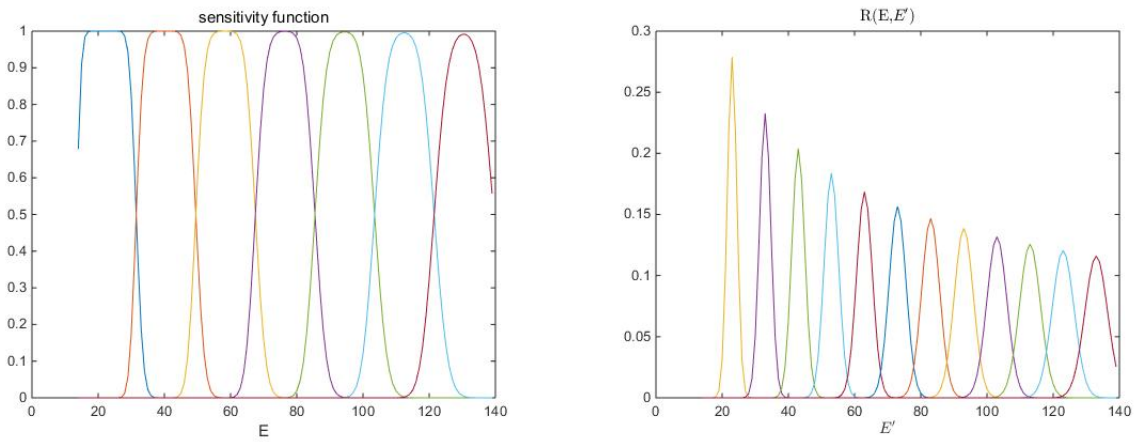

(a) sensitivity function

(b) Gaussian response function

Figure 4: Sensitivity function determines the received spectrum for each bins and Gaussian response function describes the probability of the detected photon energy, which also determines the sensitivity function.

with the constraints:

$A_c^i \geq 0 \quad \text{and} \quad A_p^i \geq 0$

where m_L^i and m_H^i represent the log-normalized measured projections along the ith path for low and high energy spectra respectively. $K_L(\theta^i)$ and $K_H(\theta^i)$ mean the log-normalized modeled projection derived from the linear relationship between μ and A_c, A_p (Eq.12), which are:

$$K_l(\theta^i) = -ln\big[\int S_l(E)exp(-A_c^i f_{KN}(E) - A_p^i f_p(E))dE\big] + ln\int S_l(E)dE \tag{14}$$

where l represents lth energy bin. Therefore, the meaning of Eq.13 is finding A_c and A_p that minimizes this cost function.

By using least square error, we can generalize Eq.13 to multiple energies situation. Different from the dual energy, multi-energy has more than two items in the cost function that needs to be minimized because the spectrum is separated into multiple bins and each bin corresponds to one projection. Thus for multiple energies, the least squares minimization problem is:

$$\theta^i = \arg\min_{\theta^i} \underbrace{\sum_{l=1}^{M}[K_l(\theta^i) - m_l^i]^2}_{Q_{\theta^i}} \tag{15}$$

where m_l^i represents the log-normalized measured projection along ith ray for lth energy bin and $K_l(\theta^i)$ is the log-normalized modeled projection for lth bin given θ^i. M means the number of energy bins.

To acquire θ^i that minimizes the cost function, multivariate Newton-Raphson theory can be used and Jacobian matrix for $K_l(\theta^i)$ is used to approach the solution iteratively.

1.5.2 Weighted sinogram decomposition

Eq.15 shows that we can obtain Compton and potoelectric images by minimizing least square error. However, for each bin, the noise increases with the decrease of number of photons measured, especially for the low-energy bins, whose normalized spectrum is lower than other bins. Therefore, in order to get better approximation for A_c and A_p, weighted least square error can be employed.

Bouman and Sauer [8] give the quadratic approximation of the Poisson log-likelihood function, which can be described as:

$$logP(\boldsymbol{M}=\boldsymbol{m^i}|\theta^i) \approx -\frac{1}{2}(\boldsymbol{K}(\theta^i)-\boldsymbol{m^i})^T\boldsymbol{\Sigma}(\boldsymbol{K}(\theta^i)-\boldsymbol{m^i})+\boldsymbol{c}(\theta^i) \tag{16}$$

where $\boldsymbol{\Sigma}$=diag$\{\boldsymbol{w}\}$ and w is the number of counts. Vector $\boldsymbol{K}(\theta^i)$ is the M dimensional column vector of log-normalized mean values determined by $\theta^i=\left[A_c^i, A_p^i\right]$ for different bins while $\boldsymbol{m^i}$ is the M dimensional column vector of log-normalized measured projections. Therefore, here we utilize the weighting given by Bouman and Sauer to minimize the error term (Eq. 17).

$$(\theta^i) = \arg\min_{\theta^i} (\boldsymbol{K(\theta^i)}-\boldsymbol{m^i})^T\boldsymbol{\Sigma}(\boldsymbol{K(\theta^i)}-\boldsymbol{m^i}) \tag{17}$$

In order to make it comparable to Eq.15, it can also be written as following expansion:

$$\theta^i = \arg\min_{\theta^i} \underbrace{\sum_{l=1}^{M} w_l^i[K_l(\theta^i)-m_l^i]^2}_{Q_{\theta^i}} \tag{18}$$

where w_l^i is the number of photon counts detected at lth bin for the ith ray.

This weighting makes sense because the photon counts reduce the variance of measured transmission projection and weighting matrix $\boldsymbol{\Sigma}$ gives more weight to the item whose measured photon count is larger, namely, noise is less.

1.5.3 MSE and the number of bins

The relation between the number of bins and their corresponding mean square error (MSE) was also explored for the phantoms with medium and high attenuation to demonstrate how the number of bin influences the reconstructed results and also how the amount of metal affects the image quality. In order to reduce the variance of samples, for each bin number, 30 samples of sinogram decompositions corresponding to the bin number were generated to reconstruct the Compton and PE images. In other word, each sample was utilized to make one Compton image and one PE image. Totally, 30 Compton and 30 photoelectric images were produced for each bin number. MSEs for both Compton and PE images derived from each sample were then computed and the average MSE was calculated. In the simulation, the bin number starts from 2 to 50 to show the trends of MSE with the incremental number of bins.

Because the appearance of aluminum will affect not only the Compton and PE reconstruction of aluminum, but also the region that is outside the aluminum. Therefore, we separated the phantom into two regions, called Al region and non-Al region. MSE of each region was measured respectively to show how aluminum influences the objects that surround it.

1.5.4 Filtered backprojection (FBP) reconstruction

Because the traditional backprojection reconstructs the image by simply summing the backprojections, the blurring will appear around the object. The region of object has the strongest amplitude because all the backprojections overlap in that region. The region around the object is less bright due to less backprojections covering there, which results in the blurring.

In order to improve the image quality, people usually employ the filtered backprojection (FBP) method [9]. Blurring can be considerably reduced by taking advantage of the relationship between 1D Fourier transform of a projection and 2D Fourier transform of the original image, which is called *Fourier-Slice Theorem* and shown below.

Table 2: PSNR for different sceneries. Left column is PSNR for Compton reconstruction and right column is for PE reconstruction. 'Mismatch' means using ideally divided multi-bins spectrum to recover Compton and PE and 'match' means using realistic spectrum to recover.

	SwDE (poi+gau)		**ideal DE** (poi+gau)		**real 7 bin** (poi,match)		**ideal 7 bin** (poi)		**real 7 bin** (mismatch)	
High, no weight	14.35	14.22	27.59	24.73	51.57	47.02	48.01	43.52	35.17	30.62
High, weighting	33.30	28.53	45.78	35.40	74.70	71.08	74.60	71.28	49.80	49.05
Medium, no weight	27.56	29.18	31.47	29.20	65.20	71.45	74.05	77.41	49.49	46.62
Medium, weighting	45.19	47.44	54.58	53.47	80.23	84.72	80.21	84.53	53.75	53.83
Low, no weight	46.50	50.86	55.12	55.67	64.42	71.42	78.66	85.21	59.06	60.13
Low, weighting	46.52	50.90	55.12	55.71	80.66	86.75	80.87	87.06	60.13	62.54

$$\begin{aligned} G(\omega,\theta) &= \left[\int_{-\infty}^{\infty}\int_{-\infty}^{\infty} f(x,y)e^{-j2\pi(ux+vy)}dxdy\right]_{u=\omega cos\theta;v=\omega sin\theta} \\ &= F[u,v]_{u=\omega cos\theta;v=\omega sin\theta} \end{aligned} \tag{19}$$

Eq.19 demostrates the Fourier transform (FT) of the projection integrated along the beam with angle θ and position ω in the 1D FT coordinate for the projection is equal to the value of 2D FT of the image whose location is $(\omega cos\theta, \omega sin\theta)$. Then we can recover the original image by using the *Fourier-Slice Theorem*(Eq.19) and inverse Fourier Transform, which is defined as:

$$f(x,y) = \int_0^{\pi}\int_{-\infty}^{\infty} |\omega| G(\omega,\theta) e^{j2\pi\omega(xcos\theta+ysin\theta)} d\omega d\theta \tag{20}$$

However, the appearance of ω makes Eq.20 not integrable and modification is needed. The common way to deal with the infinite amplitude of the function is windowing the ramp filter $|\omega|$ in frequency domain. Different windows can be implemented on the function, such as box window, Hamming window, etc.

Because windowing is not our focus, a simple box window is untilized for the function. Furthermore, we used parallel beam projections spaced at 180 angles from 0° to 180° in our simulation. During the Compton and PE reconstruction, FBP approach was applied to recover $a_c(x,y)$ and $a_p(x,y)$ from $A_c(\omega,\theta)$ and $A_p(\omega,\theta)$ respectively. Here $A_c(\omega^i,\theta^i)$ and $A_p(\omega^i,\theta^i)$ corresponds to A_c^i and A_p^i and an (ω^i,θ^i) pair maps to the ith ray.

1.6 Metrics

To evaluate the accuracy of Compton and photoelectric images, PSNR was employed in the test. Different from the PSNR used in image processing, no fixed maximum pixel value is defined for the Compton and photoelectric images. Thus, the maximum pixel value should be replaced by the maximum value of the true Compton or photoelectric image. Considering that the peak signal for these three phantom is generated by aluminum, we selected the value of aluminum as the peak signal for all Compton and photoelectric images, including phantoms with high, medium and low attenuation.

The minimum square error (MSE) was also selected as the metric evaluating the reconstruction results. In section 2.2, we study the MSE of a specific region in the phantom, such as aluminum region, and its influence on the PSNR of the whole phantom. Thus, this influence can be learned by using MSE.

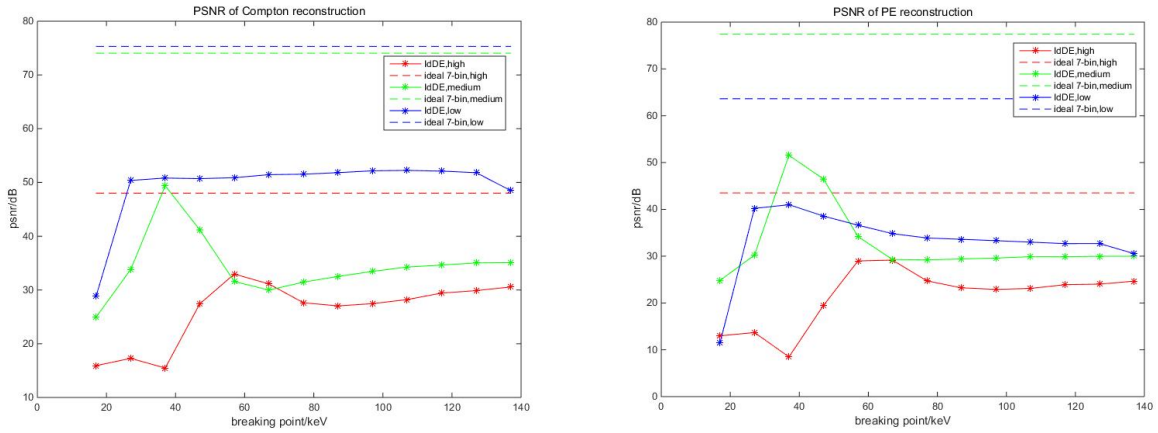

(a) PSNR of Compton reconstruction

(b) PSNR of PE image reconstruction

Figure 5: The plots show the PSNR of non-weighting Compton and PE reconstruction with the change of breaking point. Asterisks represent the breaking point of ideal DE spectrum. Dotted line means the PSNR of ideal 7-bin.

2 Results and discussion

2.1 Comparison between SwDE and weighted MECT

From Table 2, it can be seen that generally Bouman's weighting method works much better than non-weighting, especially for the phantom with high attenuation. Moreover, if we observe the table horizontally, ideal energy bin is better than the realistic one, which is modeled by E Roessl and C Herrmann [2]. In particular, the ideal dual-energy bin works better than SwDE, which manifests the potential advantage of using photon counting detector to reconstruct. Considering that there are different ways to divide the dual-energy bin (DECT), here we plot the curve of PSNR with respect to breaking point of DECT (Figure 5), showing that the breaking point will not affect our result. It can also be observed that 7-energy bin always gives rise to better results compared to DECT. Moreover, the increase of the amount of metal in the phantom also considerably deteriorates the PSNR, especially when no weighting is applied.

In our results, the combination of weighting and multi-energy photon counting detector can prominently ameliorate the reconstruction compared with the traditional SwDE. For instance, Figure 9 and 10, Figure 11 and 12, Figure 13 and 14 demonstrate the obvious advantage of multi-energy photon counting detector for high, medium and low attenuation respectively. In particular, the artifacts in Figure 9 is largely reduced.

The sensitivity of multi-energy reconstruction to errors in modeling the detector sensitivity function (Eq. 3) was also studied, in the extreme case where energy overlap was included in simulation but ignored in reconstruction. Two spectra were used to reconstruct the Compton and PE images for the simulation of multi-energy bins, abbreviated as "mismatch" and "match". Here "mismatch" means using ideally divided multi-bins spectrum (Figure 2b) to reconstruct Compton and PE image and "match" means using realistic multi-bins spectrum (Figure 3b) to reconstruct. In the comparison between "mismatch" and "match", a great improvement can be seen for "match", which reconstruct Compton and PE image using realistic multi-bins spectrum. The result of "match" method is very close to the result of ideal 7-energy bin, especially after the Bouman's weighting method. It makes sense because the sinograms of each bin are built by the same realistic multi-bins spectrum. Therefore, it is better to use the exactly same spectrum to recover Compton and PE image than using the ideally divided spectrum. However, we can do so only when given the condition that we know what type of sensor material is utilized in the photon counting detector and the probabilistic model of its spectrum is accurate for a specific device. Even with the "mismatch" spectrum, the results are

still much better than SwDE.

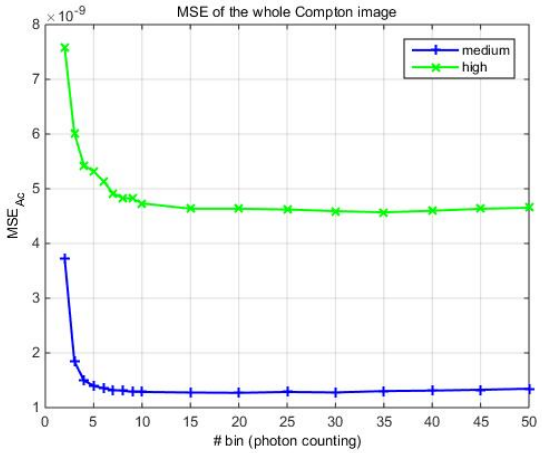

(a) MSE of the whole phantom of Compton image

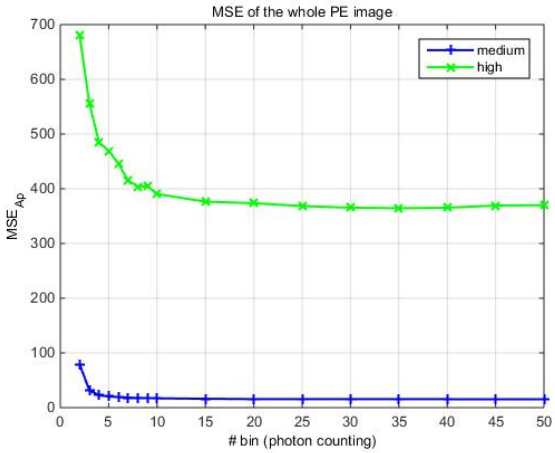

(b) MSE of the whole phantom of PE image

Figure 6: The plots show that for the whole phantom, MSE decreases with the increment of the number of bins, showing the benefit of using multi-energy bin.

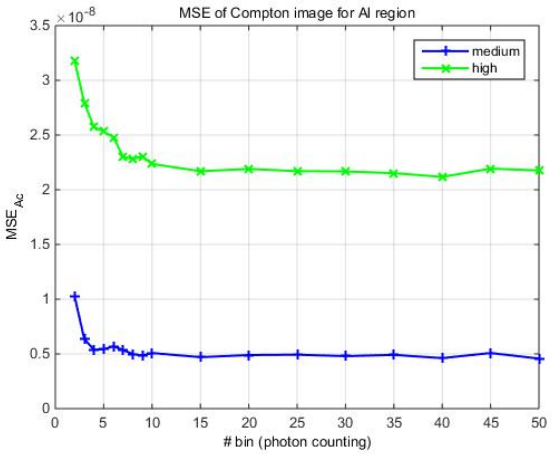

(a) MSE of Al region of Compton image

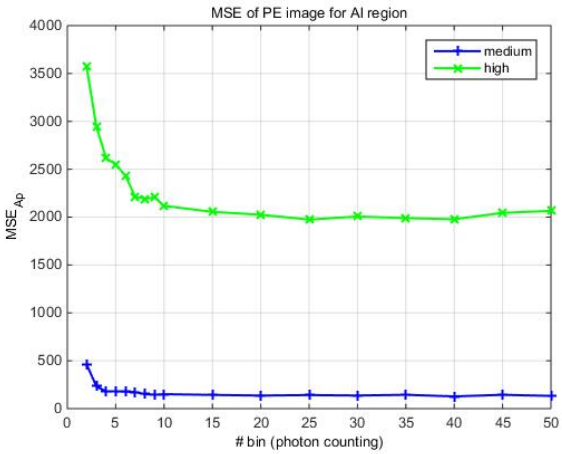

(b) MSE of Al region of PE image

Figure 7: The plots show the decrease of MSE of Al region for both Compton and PE images. The rate of the decrease of MSE also diminishes when the number of bins increases.

2.2 Multi-energy bin using photon counting detector

Compared to the SwDE, the results have shown the remarkable advantage of multi-energy bin using photon counting detector. However, it worths studying how many bins are needed to obtain a good result because the extra accuracy may entail a large amount of investment for the devices that can meet the requirement. In this case, the expense on a device will increase with the incremental number of bins.

The results from section 1.5.3 show that the increase of the number of bins can reduce the MSE especially when the bin number is less than 5 (Figure 6). However, the MSE curves finally converge to a certain value. Because continuously increasing the number of bins cannot further improve the reconstructions, it is sensible

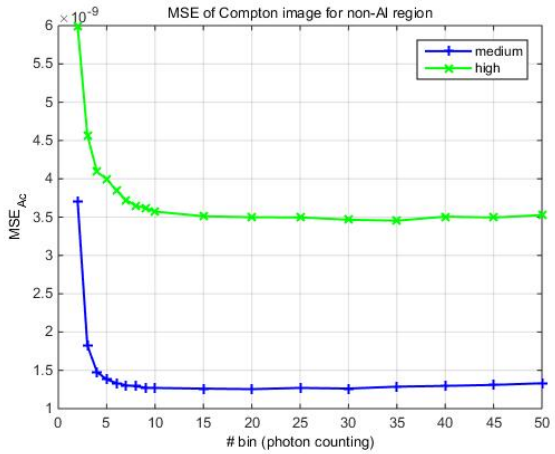

(a) MSE of non-Al region of Compton image

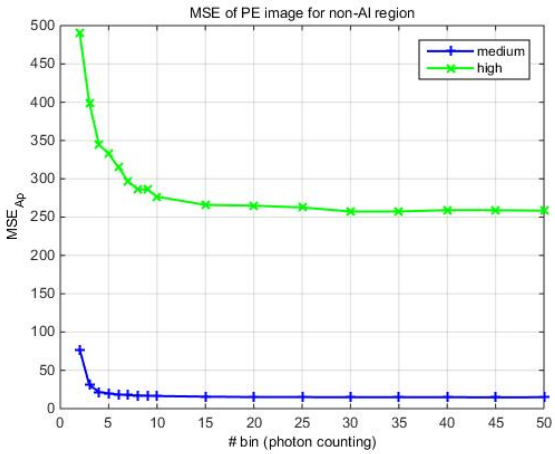

(b) MSE of non-Al region of PE image

Figure 8: The plots also show the decrease of MSE of non-Al region for both Compton and PE images. These plots demonstrate that the multi-energy bin can also reduce the noise in the region where no aluminum appears.

to pick an appropriate bin number to make a trade-off between the cost of using multi-energy bin and the improvement it can bring to us.

Figure 7 and Figure 8 show that the metal has an influence on both metal region and non-metal region. This is because the appearance of metal leads to a large number of streaks across the reconstructed images. However, the MSE of Al region is much larger than the MSE of non-Al region. Therefore, the noise of the whole reconstructed image is mainly contributed by the Al region. The MSE of non-Al region also decreases when more energy bins are applied. This means that multi-energy bin method is effective to reduce the noise not only in the Al region, but also the non-Al region which is influenced by the artifacts produced by the aluminum. The advantage of using multi-energy bin has been shown, but it is uneconomical to utilize the photon counting detector that can split the spectrum into too many bins in order to acquire a higher accuracy. Furthermore, the amount of aluminum in the phantom makes a difference to the MSE. The MSE of medium attenuation is much lower than the one of higher attenuation, which is the same as the conclusion we made in the section 2.2.

2.3 Conclusion

In this paper, we discovered that the metal in the phantom can exert a considerably negative influence on the Compton and PE reconstruction. But the use of Bouman's weighting methods can largely improve the results especially when a large amount of metal appears, which is potentially helpful for the application. Our future work will focus on the X-ray physics and the further improvement of reconstruction.

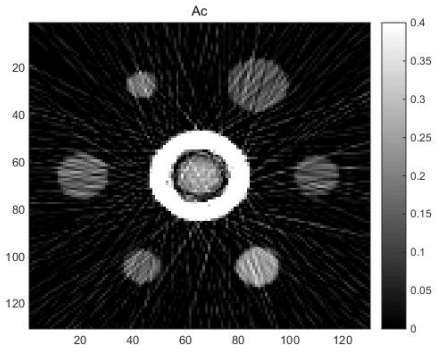

(a) Compton image

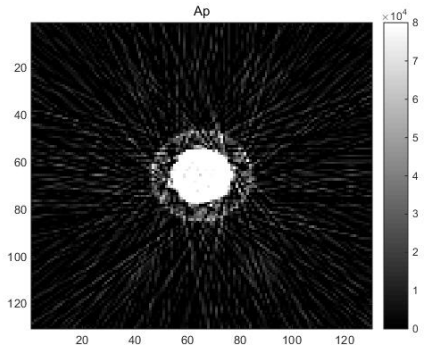

(b) PE image

Figure 9: These two plots shows the reconstruction using SwDE approach for the high attenuation phantom.

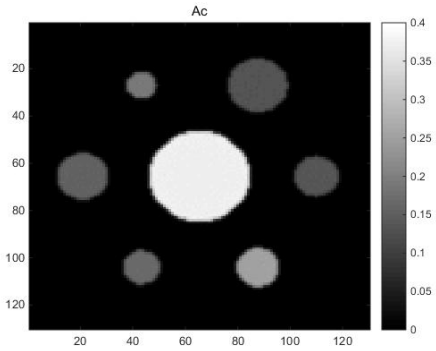

(a) Compton image

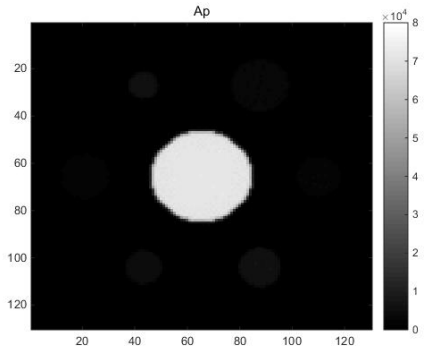

(b) PE image

Figure 10: The plots show the reconstruction using realistic 7-energy bins with weighting for high attenuation phantom.

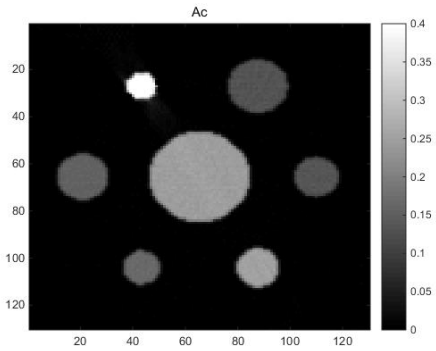

(a) Compton image

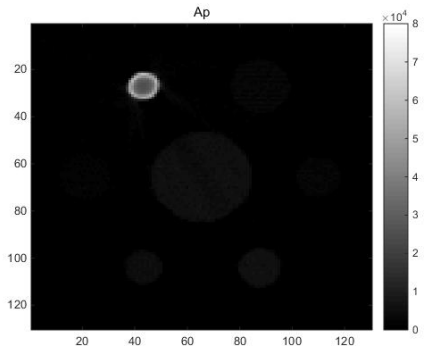

(b) PE image

Figure 11: The plots shows the reconstruction using SwDE approach for the medium attenuation phantom.

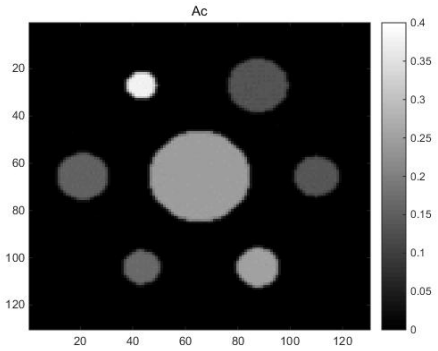

(a) Compton image

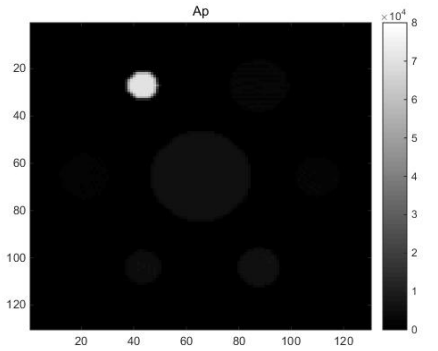

(b) PE image

Figure 12: The plots shows the reconstruction using realistic 7-energy bins with weighting for high attenuation phantom.

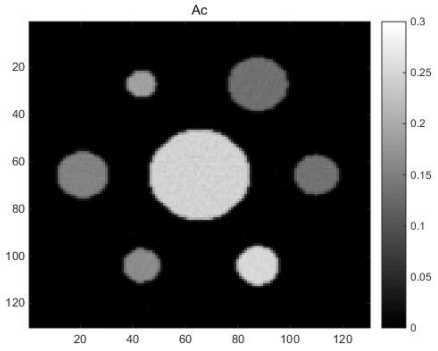

(a) Compton image

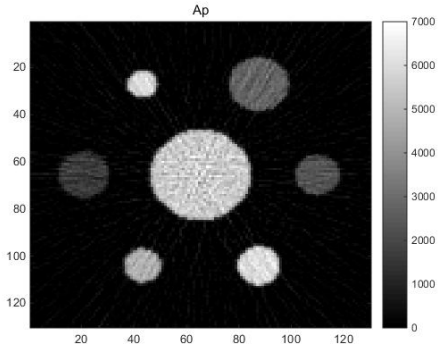

(b) PE image

Figure 13: The plots shows the reconstruction using SwDE approach for the low attenuation phantom.

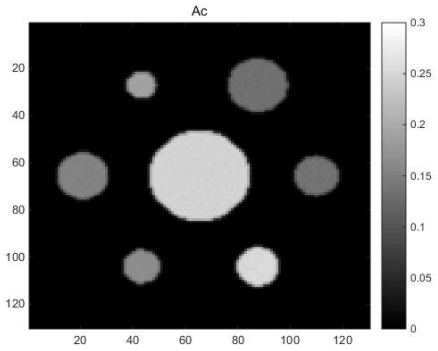

(a) Compton image

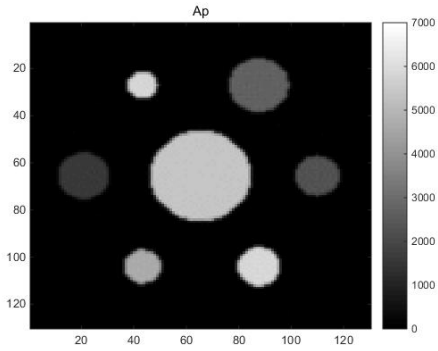

(b) PE image

Figure 14: The plots shows the reconstruction using realistic 7-energy bins with weighting for low attenuation phantom.

References

[1] Oguz Semerci, Ning Hao, Misha E Kilmer, and Eric L Miller. Tensor-based formulation and nuclear norm regularization for multienergy computed tomography. *Image Processing, IEEE Transactions on*, 23(4):1678–1693, 2014.

[2] E Roessl and C Herrmann. Cramér–rao lower bound of basis image noise in multiple-energy x-ray imaging. *Physics in medicine and biology*, 54(5):1307, 2009.

[3] Taly Gilat Schmidt, Kevin C Zimmerman, and Emil Y Sidky. The effects of extending the spectral information acquired by a photon-counting detector for spectral ct. *Physics in medicine and biology*, 60(4):1583, 2015.

[4] Oguz Semerci and Eric L Miller. A parametric level-set approach to simultaneous object identification and background reconstruction for dual-energy computed tomography. *Image Processing, IEEE Transactions on*, 21(5):2719–2734, 2012.

[5] William C Barber, Einar Nygard, Jan S Iwanczyk, Mengxi Zhang, Eric C Frey, Benjamin MW Tsui, Jan C Wessel, Nail Malakhov, Gregor Wawrzyniak, Neal E Hartsough, et al. Characterization of a novel photon counting detector for clinical ct: count rate, energy resolution, and noise performance. In *SPIE Medical Imaging*, pages 725824–725824. International Society for Optics and Photonics, 2009.

[6] Robert E Alvarez and Albert Macovski. Energy-selective reconstructions in x-ray computerised tomography. *Physics in medicine and biology*, 21(5):733, 1976.

[7] Ram Ying, Zhengrong Naidu and Carl R Crawford. Dual energy computed tomography for explosive detection. *Journal of X-ray Science and Technology*, 14(4):235–256, 2006.

[8] Charles Bouman, Ken Sauer, et al. A unified approach to statistical tomography using coordinate descent optimization. *Image Processing, IEEE Transactions on*, 5(3):480–492, 1996.

[9] Rafael C Gonzalez and Richard E Woods. Digital image processing 3rd edition, 2007.